INTERNATIONAL JOURNAL FOR NUMERICAL METHODS IN ENGINEERING
Int. J. Numer. Meth. Engng 2004; **61**:807–836 (DOI: 10.1002/nme.1086)

A three-dimensional model describing stress-temperature induced solid phase transformations: solution algorithm and boundary value problems

Ferdinando Auricchio[1, 2, *, †] and Lorenza Petrini[1]

[1]*Dipartimento di Meccanica Strutturale, Università di Pavia, Via Ferrata 1, 27100 Pavia, Italy*
[2]*Istituto di Matematica Applicata e Tecnologie Informatiche, CNR, Via Ferrata 1, 27100 Pavia, Italy*

SUMMARY

An always increasing knowledge on material properties as well as a progressively more sophisticated production technology make shape memory alloys (SMA) extremely interesting for the industrial world. At the same time, SMA devices are typically characterized by complex multi-axial stress states as well as non-homogeneous and non-isothermal conditions both in space and time.
This aspect suggests the finite element method as a useful tool to help and improve application design and realization. With this aim, we focus on a three-dimensional macroscopic thermo-mechanical model able to reproduce the most significant SMA features (*Int. J. Numer. Methods Eng*. 2002; **55**:1255–1264), proposing a simple modification of such a model. However, the suggested modification allows the development of a time-discrete solution algorithm, which is more effective and robust than the one previously discussed in the literature.
We verify the computational tool ability to simulate realistic mechanical boundary value problems with prescribed temperature dependence, studying three SMA applications: a spring actuator, a self-expanding stent, a coupling device for vacuum tightness. The effectiveness of the model to solve thermo-mechanical coupled problems will be discussed in a forthcoming work. Copyright © 2004 John Wiley & Sons, Ltd.

KEY WORDS: shape memory alloys; stress-temperature induced solid phase transformation; 3D constitutive model; numerical implementation; boundary value problems; spring actuator; self-expanding stent; vacuum tight flange

1. INTRODUCTION

Following standard literature (see among others References [1–6] and references therein), Shape memory alloys (SMA) are materials which show stress-temperature induced athermal

*Correspondence to: Ferdinando Auricchio, Dipartimento di Meccanica Strutturale, Università di Pavia, Via Ferrata 1, 27100 Pavia, Italy.
†E-mail: auricchio@unipv.it

Contract/grant sponsor: Ministero dell'istruzione, dell'università e della ricerca (MIUR)

Received 19 May 2003
Published online 23 August 2004 *Revised 6 October 2003*
 Accepted 29 January 2004

diffusionless thermoelastic martensitic transformations between two solid phases: the austenite (A), characterized by an high symmetric crystallographic configuration, and the martensite (M), characterized by a low symmetric crystallographic configuration.

At the microscopic level, we may distinguish between stress-free and stress-induced martensite. In particular, the stress-free martensite is characterized by a twinned multi-variant (MV) crystallographic structure, which minimizes the misfit with the surroundings; on the other hand, the stress-induced martensite aligns variants along a predominant direction, assuming the typical detwinned configuration characterized by a single variant (SV). Moreover, for the case of a stress-free material, it is convenient to introduce the starting and finishing temperatures of the exothermic forward transformation ($A \rightarrow M$), indicated, respectively, as M_s and M_f, as well as the starting and finishing temperatures of the endothermic reverse transformation ($M \rightarrow A$), indicated respectively as A_s and A_f. Clearly, the martensite is stable at temperatures below M_f, while the austenite is stable at temperatures above A_f, with in general $M_f < A_f$.

At the macroscopic level, depending on the temperature, SMA show two different behaviours, the shape memory effect and the pseudo-elasticity, briefly discussed in the following:

- *Shape memory effect* (*SME*): At temperatures below M_f and under mechanical loading, the multi-variant martensite transforms into product phase (SV) inducing a macroscopic deformation indicated as *transformation strain*. Since the product phase is stable at temperatures below M_f, the associated transformation strain is not recovered removing the load. Once removed the load, heating the material above A_f, the $SV \rightarrow A$ phase transformation induces the transformation strain recovery. After cooling the material below M_f, the $A \rightarrow MV$ transformation takes place without macroscopic strain generation.
- *Pseudo-elasticity* (*PE*): At temperatures above A_f and under mechanical loading, the austenite transforms into product phase (SV) inducing a macroscopic deformation indicated as *transformation strain*. Since the product phase is not stable at temperatures above A_f, upon unloading the inverse phase transformation takes place and the transformation strain is recovered.

It is important to observe that the effective material response shows a strong thermo-mechanical coupling. A first evidence of this coupling is, for example, the fact that for both the shape memory effect and the pseudo-elastic effect the stress level at which the phase transformation starts (*critical stress*) depends on the temperature with an approximately linear relationship [7, 8]. Moreover, the latent heat release/absorption associated with the phase transformations as well as the body thermal exchange with the surroundings may strongly influence the body temperature [9, 10]; a well known example is the apparent strain rate-dependence of shape-memory materials in the pseudo-elastic range [11]. These observations suggest that the thermomechanical coupling cannot be neglected to appropriately understand and describe SMA features [12–14].

Contemporarily to experimental investigations, in the last 20 years a big effort has been also devoted to define constitutive models able to describe the main SMA behaviours. From the initial phenomenological macroscopic 1D models [15, 16] to the more recent sophisticated 3D models able to take into account for example phase interactions as well as the thermomechanical coupling (for a review see Reference [17] and references therein), many progress have been achieved.

At the same time, the industrial interest has also grown and nowadays SMA are used to produce medical devices, connectors, earthquake energy-dissipation devices, aerospace and automotive actuators [18–21]. However, the realization of complex SMA devices and, even

more, the use of SMA elements to realize hybrid smart composites may induce complex multi-axial stress states in the material as well as non-isothermal conditions both in space and time. All these considerations suggest the finite element method as a useful tool to help and improve application design and realization.

Accordingly, among the models proposed in the literature we focus on the three-dimensional thermo-mechanical model proposed in Reference [22]. Without the claim to be complete and exhaustive, the model is able to catch the most significant SMA macroscopic features: the shape memory effect, the pseudo-elastic effect, the asymmetric tension–compression response, the thermo-mechanical coupling.

Henceforth, our goal is the development of a robust integration algorithm to be adopted into a finite element code for the analysis of realistic applications. In particular, for the model under investigation we propose a simple regularization of the transformation strain norm. Such a modification allows for the development of a solution algorithm, which is simpler, more effective and robust than the one previously discussed in the literature [23].

In particular, we concentrate on pure mechanical problem, through the description of the time discrete algorithm and its application to solve boundary value problems with prescribed temperature dependence (i.e. boundary value problems for which the temperature is not an independent variable). The thermo-mechanical coupling will be the subject of a forthcoming paper, in which also the behaviour of hybrid composite will be formulated and discussed.

Finally, the present paper is organized as follows. Section 2 starts with a description of the time-continuous 3D phenomenological model, summarizing the proposed time-discrete counterpart, a solution algorithm as well as the consistent tangent matrix. Section 3 presents uni-axial as well as multi-axial non-proportional tests in order to check the numerical algorithm capability and efficiency. In Section 4, adopting a finite element discretization, we simulate the behaviour of three SMA devices: a spring actuator, a self-expanding stent and a coupling device for vacuum tightness.

2. 3D PHENOMENOLOGICAL MODEL FOR STRESS-TEMPERATURE INDUCED SOLID PHASE TRANSFORMATION

Following References [22, 23], we adopt a 3D constitutive model developed within the framework of phenomenological continuum thermomechanics [24] and able to describe the main SMA macroscopic behaviours. We now discuss the time-continuous model and its time-discrete counterpart.

2.1. Time-continuous model

The model assumes the strain, $\boldsymbol{\varepsilon}$, and the absolute temperature, T, as control variables and the second-order transformation strain tensor, $\mathbf{e}^{\mathrm{tr}}$, as internal variable. The quantity $\mathbf{e}^{\mathrm{tr}}$ has the role of describing the strain associated to the phase transformations; moreover, we assume it to be traceless, following experimental evidences [25] indicating no volume changes during the phase transition. It is appropriate to observe that, dealing from now on with only a single internal variable second-order tensor, at most the model may distinguish between a generic parent phase (not associated to any macroscopic strain) and a generic product phase (associated to a

macroscopic strain). Moreover, indicating with ε_L the maximum transformation strain reached at the end of the transformation during an uniaxial test, we require:

$$0 \leqslant \|\mathbf{e}^{tr}\| \leqslant \varepsilon_L \tag{1}$$

where ε_L can be regarded as a material parameter.

Assuming a small strain regime[‡], we express the free energy function Ψ for a polycrystalline SMA material through the following convex potential:

$$\Psi(\boldsymbol{\varepsilon}, \mathbf{e}^{tr}, T) = \Psi_{el} + \Psi_{ch} + \Psi_{tr} + \Psi_{id} + \mathscr{I}_{\varepsilon_L}(\mathbf{e}^{tr}) \tag{2}$$

In particular, indicating with $\mathbf{1}$ the second-order identity tensor[§] and introducing the standard decomposition:

$$\boldsymbol{\varepsilon} = \frac{\theta}{3}\mathbf{1} + \mathbf{e}$$

where θ and $\mathbf{e}$ are, respectively, the volumetric and the deviatoric components of the total strain, we adopt the following positions:

1. the elastic strain energy Ψ_{el}, due to the thermo-elastic material deformation, is set equal to:

$$\Psi_{el} = \tfrac{1}{2} K\theta^2 + G\|\mathbf{e} - \mathbf{e}^{tr}\|^2 - 3\alpha K\theta(T - T_0) \tag{3}$$

   with K the bulk modulus, G the shear modulus, α the thermal expansion coefficient, T_0 a reference temperature;
2. the chemical energy Ψ_{ch}, due to the thermally-induced martensitic transformation, is set equal to:

$$\Psi_{ch} = \beta\langle T - M_f\rangle\|\mathbf{e}^{tr}\| \tag{4}$$

   with β a material parameter related to the dependence of the critical stress on the temperature and $\langle\bullet\rangle$ the positive part of the argument;
3. the transformation strain energy Ψ_{tr}, due to the transformation-induced hardening, is set equal to:

$$\Psi_{tr} = \tfrac{1}{2} h\|\mathbf{e}^{tr}\|^2 \tag{5}$$

   with h a material parameter defining the slope of the linear stress-transformation strain relation in the uni-axial case;

[‡]The use of the small deformation theory can be justified if one considers that in many applications large displacements but small strains are induced [26].

[§]In the following the notation $\mathbb{A}$ is used for a general fourth-order tensor, while $\mathbf{A}$ indicates a second-order tensor. $\mathbb{I}$ and $\mathbf{1}$ indicate the fourth- and the second-order identity tensor, respectively.

4. the free energy Ψ_{id}, due to the change in temperature with respect to the reference state ($T = T_0$) in an incompressible ideal solid, is set equal to:

$$\Psi_{\mathrm{id}} = (u_0 - T\eta_0) + c\left[(T - T_0) - T\ \ln\ \frac{T}{T_0}\right] \tag{6}$$

with c the heat capacity, u_0 and η_0 the internal energy and the entropy at the reference state, respectively;

5. $\mathscr{I}_{\varepsilon_{\mathrm{L}}}(\mathbf{e}^{\mathrm{tr}})$ is set equal to an indicator function introduced to satisfy the constraint on the transformation strain norm:

$$\mathscr{I}_{\varepsilon_{\mathrm{L}}}(\mathbf{e}^{\mathrm{tr}}) = \begin{cases} 0 & \text{if } \|\mathbf{e}^{\mathrm{tr}}\| \leqslant \varepsilon_{\mathrm{L}} \\ +\infty & \text{if } \|\mathbf{e}^{\mathrm{tr}}\| > \varepsilon_{\mathrm{L}} \end{cases} \tag{7}$$

Following standard arguments, we can derive the constitutive equations:

$$\begin{aligned} p &= \frac{\partial \psi}{\partial \theta} = K[\theta - 3\alpha(T - T_0)] \\ \mathbf{s} &= \frac{\partial \psi}{\partial \mathbf{e}} = 2G(\mathbf{e} - \mathbf{e}^{\mathrm{tr}}) \\ \eta &= -\frac{\partial \psi}{\partial T} = \eta_0 + 3\alpha K\theta - \beta\|\mathbf{e}^{\mathrm{tr}}\|\frac{\langle T - M_{\mathrm{f}}\rangle}{|T - M_{\mathrm{f}}|} + c\ \ln\ \frac{T}{T_0} \\ \mathbf{X} &= -\frac{\partial \psi}{\partial \mathbf{e}^{\mathrm{tr}}} = \mathbf{s} - \left[\beta\langle T - M_{\mathrm{f}}\rangle + h\|\mathbf{e}^{\mathrm{tr}}\| + \frac{\partial \mathscr{I}_{\varepsilon_{\mathrm{L}}}(\mathbf{e}^{\mathrm{tr}})}{\partial \|\mathbf{e}^{\mathrm{tr}}\|}\right]\frac{\partial \|\mathbf{e}^{\mathrm{tr}}\|}{\partial \mathbf{e}^{\mathrm{tr}}} \end{aligned} \tag{8}$$

where: p and $\mathbf{s}$ are, respectively, the volumetric and the deviatoric part of the stress $\boldsymbol{\sigma}$; η is the entropy; $\mathbf{X}$ is the thermodynamic force associated to the transformation strain and indicated in the following as *transformation stress*. The subdifferential of the indicator function results [27]:

$$\frac{\partial \mathscr{I}_{\varepsilon_{\mathrm{L}}}(\mathbf{e}^{\mathrm{tr}})}{\partial \|\mathbf{e}^{\mathrm{tr}}\|} = \begin{cases} 0 & \text{if } \|\mathbf{e}^{\mathrm{tr}}\| < \varepsilon_{\mathrm{L}} \\ +\mathcal{R} & \text{if } \|\mathbf{e}^{\mathrm{tr}}\| = \varepsilon_{\mathrm{L}} \\ \emptyset & \text{if } \|\mathbf{e}^{\mathrm{tr}}\| > \varepsilon_{\mathrm{L}} \end{cases} \tag{9}$$

We may note that Equation $(8)_4$ can be rewritten as:

$$\mathbf{X} = \mathbf{s} - \boldsymbol{\alpha} \tag{10}$$

where

$$\boldsymbol{\alpha} = [\beta\langle T - M_{\mathrm{f}}\rangle + h\|\mathbf{e}^{\mathrm{tr}}\| + \gamma]\frac{\partial \|\mathbf{e}^{\mathrm{tr}}\|}{\partial \mathbf{e}^{\mathrm{tr}}} \tag{11}$$

with

$$\begin{aligned} &\gamma = 0 \quad \text{if} \quad 0 \leqslant \|\mathbf{e}^{\mathrm{tr}}\| < \varepsilon_{\mathrm{L}} \\ &\gamma \geqslant 0 \quad \text{if} \quad \|\mathbf{e}^{\mathrm{tr}}\| = \varepsilon_{\mathrm{L}} \end{aligned} \tag{12}$$

Accordingly, the tensor $\boldsymbol{\alpha}$ plays a role similar to the so-called *back-stress* in classical plasticity and $\mathbf{X}$ can be identified as a *relative stress*. Moreover, in Equation (11) the terms $\beta\langle T - M_f\rangle$ and $h\|\mathbf{e}^{tr}\|$ describe, respectively, a piecewise linear dependency of $\boldsymbol{\alpha}$ on the temperature and a linear hardening behaviour proportional to $\|\mathbf{e}^{tr}\|$ during the phase transformation.

We complete the model introducing the associative evolution law for $\mathbf{e}^{tr}$:

$$\dot{\mathbf{e}}^{tr} = \dot{\zeta}\,\frac{\partial F(\mathbf{X})}{\partial \boldsymbol{\sigma}} \tag{13}$$

and the Kuhn–Tucker conditions

$$\dot{\zeta} \geqslant 0, \quad F \leqslant 0, \quad \dot{\zeta} F = 0$$

where F plays the role of a limit function and $\dot{\zeta}$ plays a role similar to the plastic consistent parameter.

Numerous experimental tests show an asymmetric behaviour of SMA in tension and compression [25, 28] and suggest to describe SMA as an isotropic material with a Prager-Lode type limit surface [29, 30]. Accordingly, we assume the following yield function:

$$F(\mathbf{X}) = \sqrt{2J_2} + m\,\frac{J_3}{J_2} - R \tag{14}$$

where J_2 and J_3 are the second and the third invariant of the deviatoric tensor $\mathbf{X}$, defined, respectively, as:

$$J_2 = \tfrac{1}{2}\,(\mathbf{X}^2 : \mathbf{1}), \quad J_3 = \tfrac{1}{3}\,(\mathbf{X}^3 : \mathbf{1})$$

while R is the radius of the elastic domain in the deviatoric space and m is a material parameter with $m \leqslant 0.46$ to guarantee the limit surface convexity [31]. The quantities R and m can be related to the uniaxial critical stress in tension σ_t and in compression σ_c by the relations:

$$R = 2\sqrt{\frac{2}{3}}\,\frac{\sigma_c \sigma_t}{\sigma_c + \sigma_t} \quad m = \sqrt{\frac{27}{2}}\,\frac{\sigma_c - \sigma_t}{\sigma_c + \sigma_t} \tag{15}$$

We conclude the model description, summarized in Table I, highlighting its main properties. In particular, we consider disadvantages of the model the following aspects:

- The model does not take into account the dependency of some material parameters on the specific austenite–martensite phase mixture. As an example, the model does not describe the difference between the elastic modulus of the austenite and the elastic modulus of the martensite.
- As pointed out at the beginning of the section, dealing with only a single internal variable second-order tensor, at most the model may distinguish between a generic parent phase (not associated to any macroscopic strain) and a generic product phase (associated to a macroscopic strain). Accordingly, the model does not distinguish between the austenite and the twinned martensite, since both phases do not produce macroscopic strain. Moreover, the

Table I. Time-continuous model: constitutive equations, limit function, flow rule.

TIME-CONTINUOUS MODEL FRAME

External variable: $\boldsymbol{\varepsilon}$, T

Internal variable: $\mathbf{e}^{\mathrm{tr}}$

Constitutive equations:

$$\begin{cases} p = \dfrac{\partial \psi}{\partial \theta} = K[\theta - 3\alpha(T - T_0)] \\ \mathbf{s} = \dfrac{\partial \psi}{\partial \mathbf{e}} = 2G(\mathbf{e} - \mathbf{e}^{\mathrm{tr}}) \\ \eta = -\dfrac{\partial \psi}{\partial T} = \eta_0 + 3\alpha K\theta - \beta\|\mathbf{e}^{\mathrm{tr}}\|\dfrac{\langle T - M_{\mathrm{f}}\rangle}{|T - M_{\mathrm{f}}|} + c\ln\dfrac{T}{T_0} \\ \mathbf{X} = -\dfrac{\partial \psi}{\partial \mathbf{e}^{\mathrm{tr}}} = \mathbf{s} - [\langle\beta(T - M_{\mathrm{f}})\rangle + h\|\mathbf{e}^{\mathrm{tr}}\| + \gamma]\dfrac{\partial\|\mathbf{e}^{\mathrm{tr}}\|}{\partial \mathbf{e}^{\mathrm{tr}}} \end{cases}$$

with

$$\begin{cases} \gamma = 0 & \text{if} \quad 0 \leqslant \|\mathbf{e}^{\mathrm{tr}}\| < \varepsilon_{\mathrm{L}} \\ \gamma \geqslant 0 & \text{if} \quad \|\mathbf{e}^{\mathrm{tr}}\| = \varepsilon_{\mathrm{L}} \end{cases}$$

Limit function:

$$F(\mathbf{X}) = \sqrt{2J_2} + m\frac{J_3}{J_2} - R$$

Flow rule:

$$\dot{\mathbf{e}}^{\mathrm{tr}} = \dot{\zeta}\frac{\partial F(\mathbf{X})}{\partial \boldsymbol{\sigma}} \quad \text{with} \quad \dot{\zeta} > 0, \quad F \leqslant 0, \quad \dot{\zeta}F = 0$$

model does not provide a detailed descriptions of the single martensite variants available in a specific alloy. Hence, the model cannot describe in a *exact* form the so-called martensite reorientation process, but only in an *approximated* form as discussed later.

- The model is developed in a small strain regime.

It is clearly possible to extend the model to take into account most of the cited aspects; however, we feel that they fall outside the aim of the present work. On the other hand, we consider advantages of the model the following aspects.

- The internal variable tensorial character allows to take into account in a *approximated* form the martensite reorientation process. In fact, a material characterized by a specific tensor value of the macroscopic transformation strain $\mathbf{e}^{\mathrm{tr}}$ may experience a process such that by

$$\|\mathbf{e}^{\mathrm{tr}}\| = \text{const}, \quad \dot{\mathbf{e}}^{\mathrm{tr}} \neq \mathbf{0}$$

Accordingly, this process is associated to a constant transformation strain tensor norm, indicating the presence of a constant amount of martensite fraction in the material, and to a simple change of the transformation strain direction, describing a product phase reorientation, hence describing in an *approximated* form a martensite reorientation process.

- The model is able to describe the experimentally verified linear dependency of the critical stress on the temperature [7, 8], thanks to the factor $\beta\langle T - M_f\rangle$ in Equation (11).
- The model is thermodynamically consistent, since it satisfies the second law of thermodynamics in the form of the Clausius–Duhem inequality:

$$D = D_m + D_{th} \geqslant 0 \tag{16}$$

where the dissipation D is the sum of the mechanical dissipation D_m and of the thermal dissipation D_{th}, classically defined [24]. In fact, the assumption of a convex limit function and the respect of the normality rule assure the positiveness of the mechanical dissipation:

$$D_m = \boldsymbol{\sigma} : \dot{\boldsymbol{\varepsilon}} - \dot{\psi} - \eta\dot{T} = \mathbf{X} : \dot{\mathbf{e}}^{tr} \geqslant 0$$

while the assumption of the Fourier's law for heat conduction $\mathbf{q} = -K^{th}\nabla T$, with a positive thermal isotropic conductivity parameter K^{th}, assures the positiveness of the thermal dissipation:

$$D_{th} = -\frac{\mathbf{q}}{T} \cdot \nabla T \geqslant 0$$

where $\mathbf{q}$ is the heat flux vector and ∇ indicates the gradient operator.

- The model falls into the class of dissipative model. However, assuming the magnitude of the thermodynamic force $\mathbf{X}$ equal to zero, the model behaves as a non-dissipative one [32]. Accordingly, the model is able to describe some experimental results [33], showing that in certain situations the pseudo-elastic hysteretic behaviour is mainly due to non-dissipative endo–exothermic reactions.

2.2. Time-discrete frame and solution algorithm

We now treat the non-linear problem described in Section 2.1 as an implicit time-discrete strain-driven problem. Accordingly, we subdivide the time interval of interest $[0, T]$ in sub-increments and we wish to solve the evolution problem over the generic interval $[t_n, t]$ with $t > t_n$.

Known the solution at the time t_n and the strain tensor at the time t, an implicit backward Euler methods is used to integrate the model rate equations; the stress history is then derived from the strain history by means of a procedure known as *return-map* [34–36].

From now on we limit the discussion only to problems for which we assume the temperature constant and given during each time-step. Accordingly, we are required to solve only the mechanical part of the model, assuming at every instant the temperature to be given, eventually variable in time and space during the analysis but constant during each time-step.

2.2.1. Time integration. The time-discrete counterpart of the constitutive model is:

$$
\begin{aligned}
&p = K[\theta - 3\alpha(T - T_0)]\\
&\mathbf{s} = 2G(\mathbf{e} - \mathbf{e}^{\mathrm{tr}})\\
&\mathbf{X} = \mathbf{s} - [\beta\langle T - M_{\mathrm{f}}\rangle + h\|\mathbf{e}^{\mathrm{tr}}\| + \gamma]\,\frac{\partial\|\mathbf{e}^{\mathrm{tr}}\|}{\partial\mathbf{e}^{\mathrm{tr}}}\\
&\gamma \geqslant 0\\
&\mathbf{e}^{\mathrm{tr}} = \mathbf{e}_n^{\mathrm{tr}} + \Delta\zeta\,\frac{\partial F(\mathbf{X})}{\partial\boldsymbol{\sigma}}\\
&\|\mathbf{e}^{\mathrm{tr}}\| \leqslant \varepsilon_{\mathrm{L}}\\
&F(\mathbf{X}) = \sqrt{2J_2} + m\,\frac{J_3}{J_2} - R \leqslant 0\\
&\Delta\zeta \geqslant 0 \quad \Delta\zeta F(\mathbf{X}) = 0
\end{aligned}
\tag{17}
$$

where $\Delta\zeta = (\zeta - \zeta_n)$ is the consistency parameter, time integrated over the interval $[t_n, t]$.

From a computational standpoint the time-discrete model as presented in Equation (17) shows a major problem, since the transformation stress $\mathbf{X}$ depends on the derivative of the transformation strain (Equation $(17)_3$) which can be null making the derivative undefined. To overcome this difficulty different approaches can be followed [23, 37]. Herein, we propose to substitute the Euclidean norm $\|\mathbf{e}^{\mathrm{tr}}\|$ with the regularized norm $\overline{\|\mathbf{e}^{\mathrm{tr}}\|}$, defined as:

$$
\overline{\|\mathbf{e}^{\mathrm{tr}}\|} = \|\mathbf{e}^{\mathrm{tr}}\| - \frac{\delta^{(\delta+1)/\delta}}{\delta - 1}\,(\|\mathbf{e}^{\mathrm{tr}}\| + \delta)^{(\delta-1)/\delta} \tag{18}
$$

where δ is a user-defined parameter which controls the smoothness of the regularized norm.

For large values of $\mathbf{e}^{\mathrm{tr}}$ the regularized norm coincides with the Euclidean norm; for small values of $\mathbf{e}^{\mathrm{tr}}$ the difference between $\overline{\|\mathbf{e}^{\mathrm{tr}}\|}$ and $\|\mathbf{e}^{\mathrm{tr}}\|$ is measured by δ and it tends to zero whenever $\delta \to 0$. Moreover, the quantity $\overline{\|\mathbf{e}^{\mathrm{tr}}\|}$ is always differentiable, even for $\mathbf{e}^{\mathrm{tr}} = \mathbf{0}$ when $\delta > 0$. This means that the quantity $\partial\overline{\|\mathbf{e}^{\mathrm{tr}}\|}/\partial\mathbf{e}^{\mathrm{tr}}$ is always defined.

To give an indication on the physical meaning of the parameter δ to be helpful also in the choice of such a parameter, we may consider a process in which $\mathbf{e}^{\mathrm{tr}} \to \mathbf{0}$ along a defined direction, i.e. $\mathbf{e}^{\mathrm{tr}} = \pi\mathbf{d}$ with $\mathbf{d}$ fixed and $\|\mathbf{d}\| = 1$ while $\pi \to 0$. For such a process it is easy to show that:

$$
\lim_{\pi\to 0^+} \overline{\|\mathbf{e}^{\mathrm{tr}}\|} = \lim_{\pi\to 0^+} \left[\pi - \frac{\delta^{(\delta+1)/\delta}}{\delta - 1}\,(\pi + \delta)^{(\delta-1)/\delta}\right] = \frac{\delta^2}{1 - \delta} \tag{19}
$$

Hence, the parameter δ measures the difference between the Euclidean norm and the regularized norm at zero and, accordingly, a proper choice for δ could satisfy the following condition:

$$
\overline{\|\mathbf{0}\|} = \frac{\delta^2}{1 - \delta} \ll \varepsilon_{\mathrm{L}} \tag{20}
$$

Table II. Time-discrete frame: solution algorithm.

TIME-DISCRETE MODEL FRAME

1. Compute trial state

$$\begin{cases} \mathbf{e}^{\mathrm{tr},TR} = \mathbf{e}_n^{\mathrm{tr}} \\ \mathbf{s}^{TR} = 2G(\mathbf{e} - \mathbf{e}^{\mathrm{tr},TR}) \end{cases}$$

2. Check material state

$$\begin{cases} \text{compute:} \begin{cases} \boldsymbol{\alpha}^{TR} = [\langle \beta(T - M_{\mathrm{f}}) \rangle + h\overline{\|\mathbf{e}^{\mathrm{tr},TR}\|}] \dfrac{\partial \overline{\|\mathbf{e}^{\mathrm{tr},TR}\|}}{\partial \mathbf{e}^{\mathrm{tr}}} \\ \mathbf{X}^{TR} = \mathbf{s}^{TR} - \boldsymbol{\alpha}^{TR} \\ F^{TR} = \sqrt{2J_2(\mathbf{X}^{TR})} + m\dfrac{J_3(\mathbf{X}^{TR})}{J_2(\mathbf{X}^{TR})} - R \end{cases} \\ \text{check } F^{TR}\text{:} \begin{cases} \text{if } (F^{TR} < 0) \text{ then} & \textbf{elastic step } (EL) \\ \text{else} & \textbf{active p.t. } (PT_1) \\ \text{end if} \end{cases} \end{cases}$$

3. Update material state

See Table III

2.2.2. Solution algorithm. We approach the solution of the 'modified' time-discrete model with an elastic-predictor inelastic-corrector procedure, borrowed from the classical theory of plasticity (Table II). The algorithm consists in evaluating an elastic trial state, in which the internal variable remains constant, and in verifying the admissibility of the trial function. If the trial state is admissable, the step is elastic; if the trial state is non-admissable, the step is inelastic and the transformation strain has to be updated through integration of the evolutionary equation.

We solve the inelastic step with the following procedure (Table III):

- Assume $\gamma = 0$ and rewrite Equation (17) in the residual form as follows:

$$\begin{aligned} \mathbf{R}^X &= \mathbf{X} - \mathbf{s}^{TR} + 2G\Delta\zeta \frac{\partial F}{\partial \boldsymbol{\sigma}} + [\langle \beta(T - M_{\mathrm{f}}) \rangle + h\overline{\|\mathbf{e}^{\mathrm{tr}}\|}] \frac{\partial \overline{\|\mathbf{e}^{\mathrm{tr}}\|}}{\partial \mathbf{e}^{\mathrm{tr}}} = \mathbf{0} \\ R^{\Delta\zeta} &= \sqrt{2J_2} + m\frac{J_3}{J_2} - R = 0 \end{aligned} \tag{21}$$

  Then, solve the seven non-linear scalar equations with a Newton–Raphson method.

- If the above solution is not admissible (i.e. $\overline{\|\mathbf{e}^{\mathrm{tr}}\|} > \varepsilon_{\mathrm{L}}$), assume $\gamma > 0$ and rewrite Equation (17) in the residual form as follows:

$$\begin{aligned} \mathbf{R}^X &= \mathbf{X} - \mathbf{s}^{TR} + 2G\Delta\zeta \frac{\partial F}{\partial \boldsymbol{\sigma}} + [\langle \beta(T - M_{\mathrm{f}}) \rangle + h\overline{\|\mathbf{e}^{\mathrm{tr}}\|} + \gamma] \frac{\partial \overline{\|\mathbf{e}^{\mathrm{tr}}\|}}{\partial \mathbf{e}^{\mathrm{tr}}} = \mathbf{0} \\ R^{\Delta\zeta} &= \sqrt{2J_2} + m\frac{J_3}{J_2} - R = 0 \\ R^{\gamma} &= \overline{\|\mathbf{e}^{\mathrm{tr}}\|} - \varepsilon_{\mathrm{L}} = 0 \end{aligned} \tag{22}$$

  Then, solve the eight non-linear scalar equations with a Newton–Raphson method.

Table III. Time-discrete frame: branch solution and state detection.

BRANCH SOLUTION AND STATE UPDATE

if (CASE EL - Elastic step) then

$$\begin{cases} \mathbf{e}^{\mathrm{tr}} = \mathbf{e}^{\mathrm{tr},TR} \\ \mathbf{s} = 2G(\mathbf{e} - \mathbf{e}^{\mathrm{tr}}) \end{cases}$$

else if (CASE PT_1 - Evolving phase transformation) then

$$\begin{cases} \text{find } \mathbf{e}^{\mathrm{tr}} \text{ solving Equation (21)} \\ \text{check solution:} \quad \begin{cases} \text{if } \overline{\|\mathbf{e}^{\mathrm{tr}}\|} < \varepsilon_{\mathrm{L}} \text{ then} & \text{exit} \\ \text{else} & \textbf{CASE } PT_2 \\ \text{end if} \end{cases} \end{cases}$$

if (CASE PT_2 - Saturated phase transformation) then

find $\mathbf{e}^{\mathrm{tr}}$, γ solving Equation (22)

end if

end if

Focusing for simplicity only on the case of saturated phase transition ($\overline{\|\mathbf{e}^{\mathrm{tr}}\|} = \varepsilon_{\mathrm{L}}$), the iterative Newton–Raphson method requires the linearization of Equation (22), hence the computation of the matrix:

$$\begin{bmatrix} \mathbf{R},{}^{X}_{X} & \mathbf{R},{}^{X}_{\Delta\zeta} & \mathbf{R},{}^{X}_{\gamma} \\ \mathbf{R},{}^{\Delta\zeta}_{X} & \mathbf{R},{}^{\Delta\zeta}_{\Delta\zeta} & \mathbf{R},{}^{\Delta\zeta}_{\gamma} \\ \mathbf{R},{}^{\gamma}_{X} & \mathbf{R},{}^{\gamma}_{\Delta\zeta} & \mathbf{R},{}^{\gamma}_{\gamma} \end{bmatrix}$$

where the subscript comma indicates derivation with respect to the quantity following the comma, i.e. $\mathbf{R},{}^{X}_{X}$ means the derivation of the first six scalar equation $\mathbf{R}^{X}$ with respect to $\mathbf{X}$, and so on. The matrix coefficients are similar to the ones described in Reference [23] and, accordingly, we do not report them here.

The time-discrete model is completed by the calculus of the consistent tangent tensor which allows the quadratic convergence of the Newton–Raphson method, expressed as:

$$\mathbb{D} = \frac{\mathrm{d}\boldsymbol{\sigma}}{\mathrm{d}\boldsymbol{\varepsilon}}$$

For brevity, we only provide details on the computation of the consistent tangent for the case of the saturated phase transformation; the evolving phase transformation case can be easily deduced eliminating the term related to the γ parameter.

Recalling Equations $(8)_1$ and $(8)_2$, the linearization of the volumetric and deviatoric elastic constitutive relations gives:

$$\begin{aligned} \mathrm{d}p\mathbf{1} &= K(\mathbf{1}\otimes\mathbf{1}) : \mathrm{d}\boldsymbol{\varepsilon} \\ \mathrm{d}\mathbf{s} &= 2G\left(\mathbb{I} - \frac{\mathrm{d}\mathbf{e}^{\mathrm{tr}}}{\mathrm{d}\mathbf{e}}\right)\mathbb{I}_{\mathrm{dev}} : \mathrm{d}\boldsymbol{\varepsilon} \end{aligned} \tag{23}$$

where

$$\begin{aligned} \mathbb{I}_{\mathrm{dev}} &= \mathbb{I} - \tfrac{1}{3}(\mathbf{1}\otimes\mathbf{1}) \\ \mathrm{d}\mathbf{e} &= \mathbb{I}_{\mathrm{dev}} : \mathrm{d}\boldsymbol{\varepsilon} \end{aligned}$$

If we now consider Equation (22) as function of $\mathbf{X}$, $\Delta\zeta$, γ and $\mathbf{e}$, the corresponding linearization gives:

$$\begin{aligned} \mathrm{d}(\mathbf{R}^X) &= \mathbf{R},{}^{X}_{X} : \mathrm{d}\mathbf{X} + \mathbf{R},{}^{X}_{\Delta\zeta}\ \mathrm{d}\Delta\zeta + \mathbf{R},{}^{X}_{\gamma}\ \mathrm{d}\gamma + \mathbf{R},{}^{X}_{\mathbf{e}} : \mathrm{d}\mathbf{e}\ = \mathbf{0} \\ \mathrm{d}(R^{\Delta\zeta}) &= \mathbf{R},{}^{\Delta\zeta}_{X} : \mathrm{d}\mathbf{X} + R,{}^{\Delta\zeta}_{\Delta\zeta}\ \mathrm{d}\Delta\zeta + R,{}^{\Delta\zeta}_{\gamma}\ \mathrm{d}\gamma + \mathbf{R},{}^{\Delta\zeta}_{\mathbf{e}} : \mathrm{d}\mathbf{e} = 0 \\ \mathrm{d}(R^{\gamma}) &= \mathbf{R},{}^{\gamma}_{X} : \mathrm{d}\mathbf{X} + R,{}^{\gamma}_{\Delta\zeta}\ \mathrm{d}\Delta\zeta + R,{}^{\gamma}_{\gamma}\ \mathrm{d}\gamma + \mathbf{R},{}^{\gamma}_{\mathbf{e}} : \mathrm{d}\mathbf{e}\ = 0 \end{aligned} \tag{24}$$

where

$$\begin{aligned} \mathbf{R},{}^{X}_{\mathbf{e}} &= -2G\mathbb{I} \\ \mathbf{R},{}^{\Delta\zeta}_{\mathbf{e}} &= \mathbf{0} \\ \mathbf{R},{}^{\gamma}_{\mathbf{e}} &= \mathbf{0} \end{aligned}$$

Accordingly, we can write:

$$\begin{bmatrix} \mathrm{d}\mathbf{X} \\ \mathrm{d}\Delta\zeta \\ \mathrm{d}\gamma \end{bmatrix} = \begin{bmatrix} \mathbf{R},{}^{X}_{X} & \mathbf{R},{}^{X}_{\Delta\zeta} & \mathbf{R},{}^{X}_{\gamma} \\ \mathbf{R},{}^{\Delta\zeta}_{X} & R,{}^{\Delta\zeta}_{\Delta\zeta} & R,{}^{\Delta\zeta}_{\gamma} \\ \mathbf{R},{}^{\gamma}_{X} & R,{}^{\gamma}_{\Delta\zeta} & R,{}^{\gamma}_{\gamma} \end{bmatrix}^{-1} \begin{bmatrix} -2G\mathbb{I} \\ \mathbf{0} \\ \mathbf{0} \end{bmatrix} : \mathrm{d}\mathbf{e} \tag{25}$$

Taking advantage of Equation (25), the linearization of Equation $(17)_5$ gives:

$$\mathrm{d}(\mathbf{e}^{\mathrm{tr}}) = \mathbf{e},{}^{\mathrm{tr}}_{X} : \mathrm{d}\mathbf{X} + \mathbf{e},{}^{\mathrm{tr}}_{\Delta\zeta}\ \mathrm{d}\Delta\zeta + \mathbf{e},{}^{\mathrm{tr}}_{\gamma}\ \mathrm{d}\gamma = \mathbb{E} : \mathrm{d}\mathbf{e} \tag{26}$$

with:

$$\mathbb{E} = [\mathbf{e},{}^{\mathrm{tr}}_{X} \quad \mathbf{e},{}^{\mathrm{tr}}_{\Delta\zeta} \quad \mathbf{0}] \begin{bmatrix} \mathbf{R},{}^{X}_{X} & \mathbf{R},{}^{X}_{\Delta\zeta} & \mathbf{R},{}^{X}_{\gamma} \\ \mathbf{R},{}^{\Delta\zeta}_{X} & R,{}^{\Delta\zeta}_{\Delta\zeta} & R,{}^{\Delta\zeta}_{\gamma} \\ \mathbf{R},{}^{\gamma}_{X} & R,{}^{\gamma}_{\Delta\zeta} & R,{}^{\gamma}_{\gamma} \end{bmatrix}^{-1} \begin{bmatrix} -2G\mathbb{I} \\ \mathbf{0} \\ \mathbf{0} \end{bmatrix}$$

In conclusion, the consistent tangent tensor assumes the form:

$$\mathbb{D} = K(\mathbf{1} \otimes \mathbf{1}) + 2G(\mathbb{I} - \mathbb{E})\mathbb{I}_{\text{dev}} \tag{27}$$

3. NUMERICAL EXAMPLES: STRESS–STRAIN PROCESSES

To show the model ability to predict the main features of SMA materials as well as to start testing the efficiency of the numerical algorithm herein proposed, we consider in the following several uniaxial and bi-axial (non-proportional) stress–strain processes performed under strain, stress or temperature control. In particular, in a strain control test we specify only the prescribed strain components, requiring all the other stress components to be zero; in a stress control test we specify the prescribed stress components, requiring all the other stress components to be zero; in a temperature control test we specify the body temperature, requiring all the stress components to be zero.

Unless otherwise stated, on the basis of the experimental data presented in Reference [38], we adopt the following material properties:

$$\begin{array}{llll} E = 53000\,\text{MPa}, & h = 1000\,\text{MPa}, & \nu = 0.36, & \varepsilon_{\text{L}} = 0.04 \\ M_{\text{f}} = 223\,\text{K}, & M_{\text{s}} = 239\,\text{K}, & A_{\text{s}} = 248\,\text{K}, & A_{\text{f}} = 260\,\text{K} \\ T_0 = 245\,\text{K}, & \alpha = 10^{-6}\,\text{K}^{-1}, & \beta = 2.1\,\text{MPa}\,\text{K}^{-1}, & \delta = 0.02 \\ \sigma_{\text{c}} = 72\,\text{MPa}, & \sigma_{\text{t}} = 56\,\text{MPa}, & & \end{array}$$

assuming also to start always with a material in the parent phase (i.e. with $\|\mathbf{e}^{\text{tr}}\| = 0$).

3.1. Uniaxial tests

We start simulating tension–compression as well as torsion tests under stress control at three different temperatures, and in particular for $T > A_{\text{f}}$, $M_{\text{s}} < T < A_{\text{s}}$ and $T < M_{\text{f}}$. For the tests with $T < A_{\text{s}}$ we also investigate the shape recovery under temperature control.

Figure 1 reports the stress–strain responses with a continuous line and, for the tests with $T < A_{\text{s}}$, also the strain recovery with a dashed line. The results underline the model capability to:

- predict the pseudo-elastic effect, the shape memory effect as well as the intermediate behaviour;
- predict an asymmetric response in tension and compression.

To check the algorithm robustness we performed the tests with two different stress increments per step: in particular, we considered stress increments equal to 30 and to 3 MPa in the tension–compression tests and equal to 20 and to 2 MPa in the torsion tests. As shown in Figure 1 no effective difference can be appreciated between the results. We obtain the same good performances also for the cyclic uni-axial tension–compression and torsion tests under strain control (Figure 2).

Performing cyclic torsion tests at $T < M_{\text{f}}$ under strain control and considering materials with different hardening parameters h, we notice a peculiar behaviour: for small values of h, the material totally transforms and enters into the saturated phase transition state even if the maximum strain imposed during cycles is lower than ε_{L} (i.e. $\max|\gamma_{12}| < \varepsilon_{\text{L}}$). This

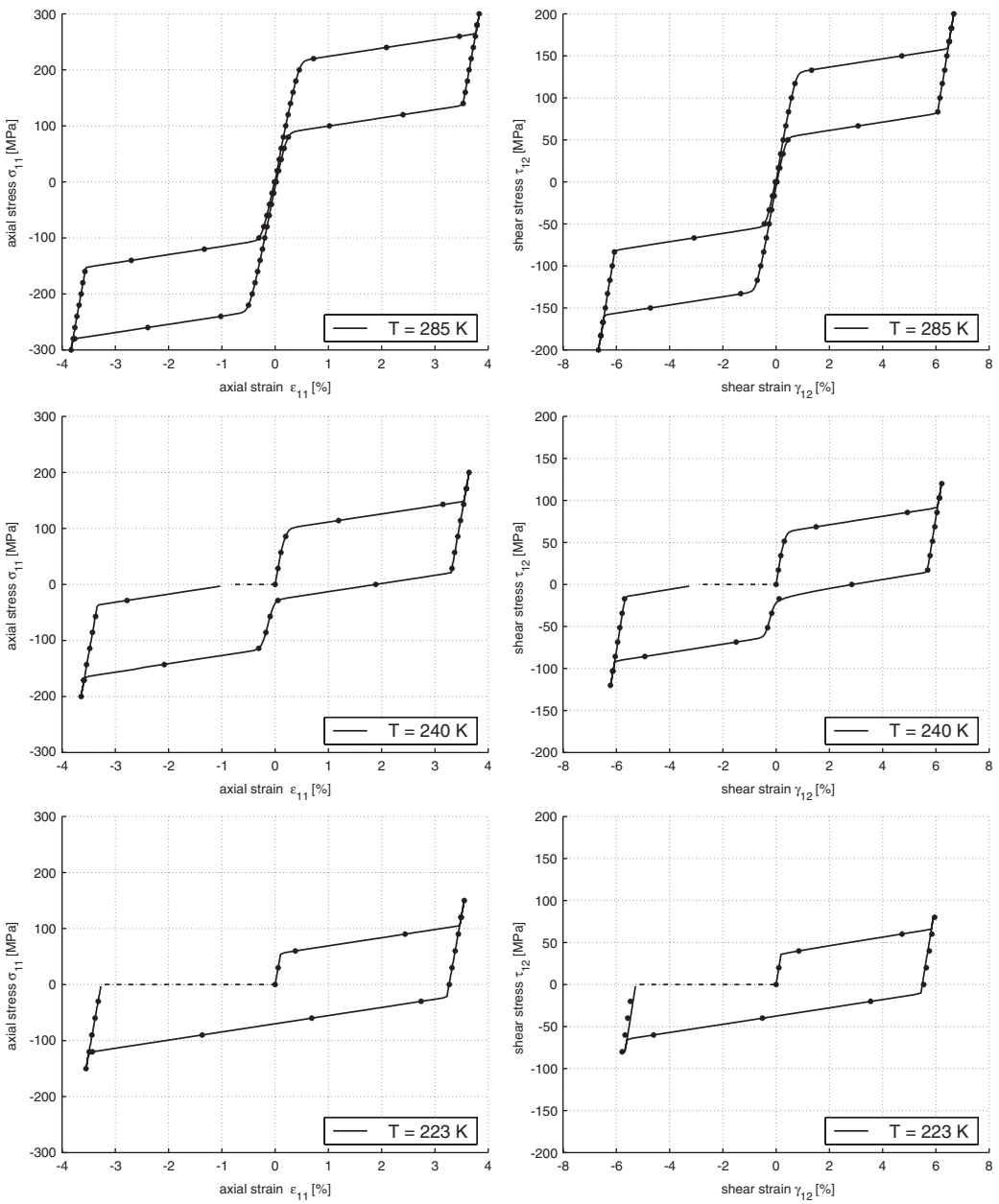

Figure 1. Tension–compression tests (left part) and torsion tests (right part) under stress control with continuous line: $T = 285$ K (upper); $T = 240$ K (centre); $T = 223$ K (lower). For $T < A_s = 248$ K strain recovery induced by a heating cycle is indicated with a dash–dot line. Stress increment per step during tension–compression tests: 3 MPa (continuous line) and 30 MPa (dot line). Stress increment per step during torsion tests: 2 MPa (continuous line) and 20 MPa (dot line).

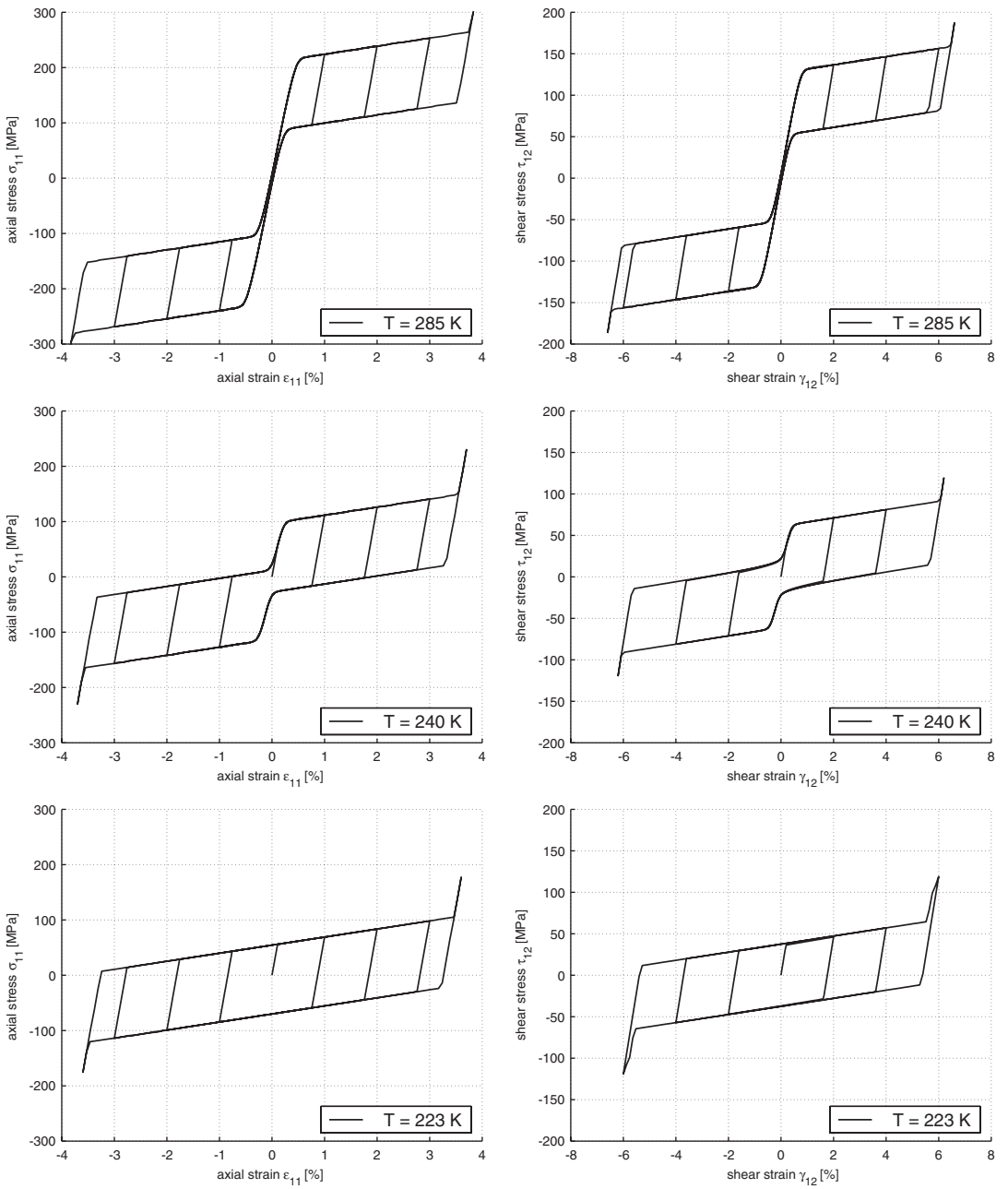

Figure 2. Cyclic tension–compression tests (left part) and torsion tests (right part) under strain control at temperature: $T = 285\,\mathrm{K}$ (upper); $T = 240\,\mathrm{K}$ (centre); $T = 223\,\mathrm{K}$ (lower).

unexpected behaviour can be explained noting that, during a torsion test in martensitic phase, the transformation strain tensor is traceless but the components on the diagonal tend to progressively increase during the cycles for the case of no hardening, while they reach a constant value for the case with hardening.

We visualize this phenomenon in Figure 3 where we compare the response for the case $h = 0$ MPa and the case $h = 1000$ MPa, under cyclic torsion test with $-3\% < \gamma_{12} < 3\%$, assuming in both cases $\varepsilon_L = 4\%$. Recalling Equation $(17)_5$, we may conclude that this peculiar phenomenon depends on the transformation criterion assumed in the model, and in particular on the limit function $F(\mathbf{X})$ introduced.

The described behaviour disappears in the pseudo-elasticity range: in this case, at the end of each loading–unloading cycle, the material has to recover all the deformation, and the components of the transformation strain tensor go back to zero.

3.2. Bi-axial tests

We verify the model efficiency also performing multi-axial non-proportional tests. In particular, we investigate two types of strain controlled bi-axial tests varying the strain components ε_{11}-γ_{12} in the range $\pm 4\%$. The first type of test consists of an hourglass-shaped strain history input, the second one consists of a square-shaped strain history input. Figure 4 shows the strain history input (upper part) and the stress history output for $T = 285\,\mathrm{K} > A_f$ (centre part) and $T = 223\,\mathrm{K} = M_f$ (lower part). Both series of tests are performed using two different time steps: 0.02 and 0.2 s.

We repeat the hourglass-shaped test and the square-shaped test also under stress control. At $T = 285$ K we vary the stress components σ_{11}-τ_{12} in the range ± 250 MPa (Figure 5). At $T = 223$ K we vary the stress components σ_{11}-τ_{12} in the range ± 100 MPa; then, at the end of the cycle, we increase the temperature up to A_f, such that the residual strain recovery takes place as shown in the lower part of Figure 6 with the dotted line.

The tests results highlight the algorithm robustness as well as the model ability to describe some SMA characteristic behaviours experimentally verified [38], in particular:

- the coupling among tension and torsion stress/strain during non-proportional loading;
- the complete reversibility of the pseudo-elastic strain during non-proportional loading–unloading mechanical cycles;
- the path dependence of the stress/strain induced by the external forces.

4. NUMERICAL EXAMPLES: BOUNDARY VALUE PROBLEMS

In the following we validate the adopted model as well as the proposed algorithm solving three boundary value problems: a spring actuator, a self-expanding stent and a vacuum coupling device.

4.1. Spring actuator

The most classical and simple SMA actuator, exploiting the shape memory effect, consists of a vertical spring loaded with a weight [39, 40]. If the stress applied by the weight at $T < M_f$ is greater than the martensitic critical stress, the transformation phase from multi-variant to

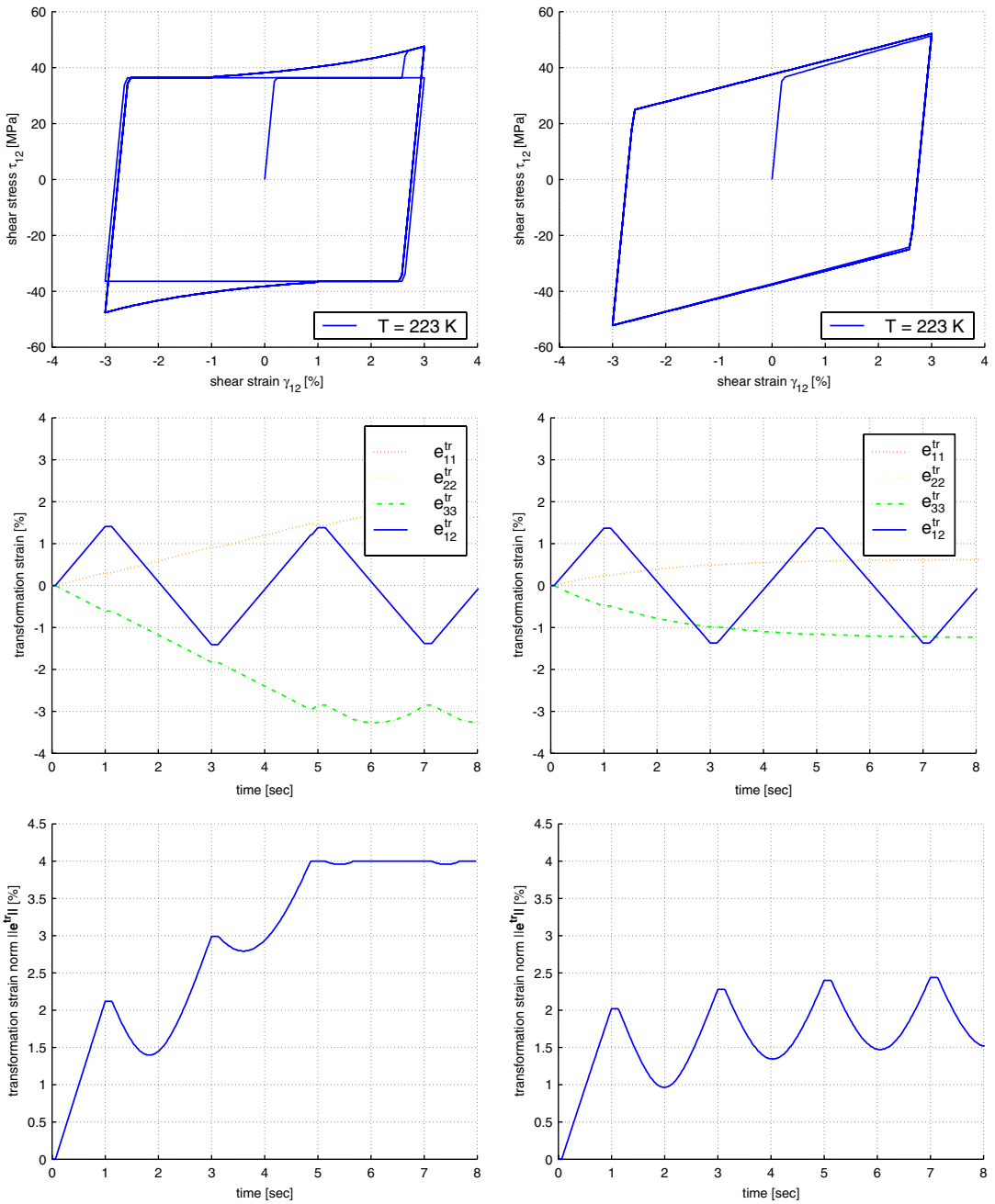

Figure 3. Cyclic torsion test under strain control up to 3% at $T = 223\,\mathrm{K}$. Linear kinematic hardening parameter $h = 0\,\mathrm{MPa}$ (left); linear kinematic hardening parameter $h = 1000\,\mathrm{MPa}$ (right). Stress τ_{12}–strain γ_{12} response (upper); transformation strain tensor components output history (centre); transformation strain norm output history (lower).

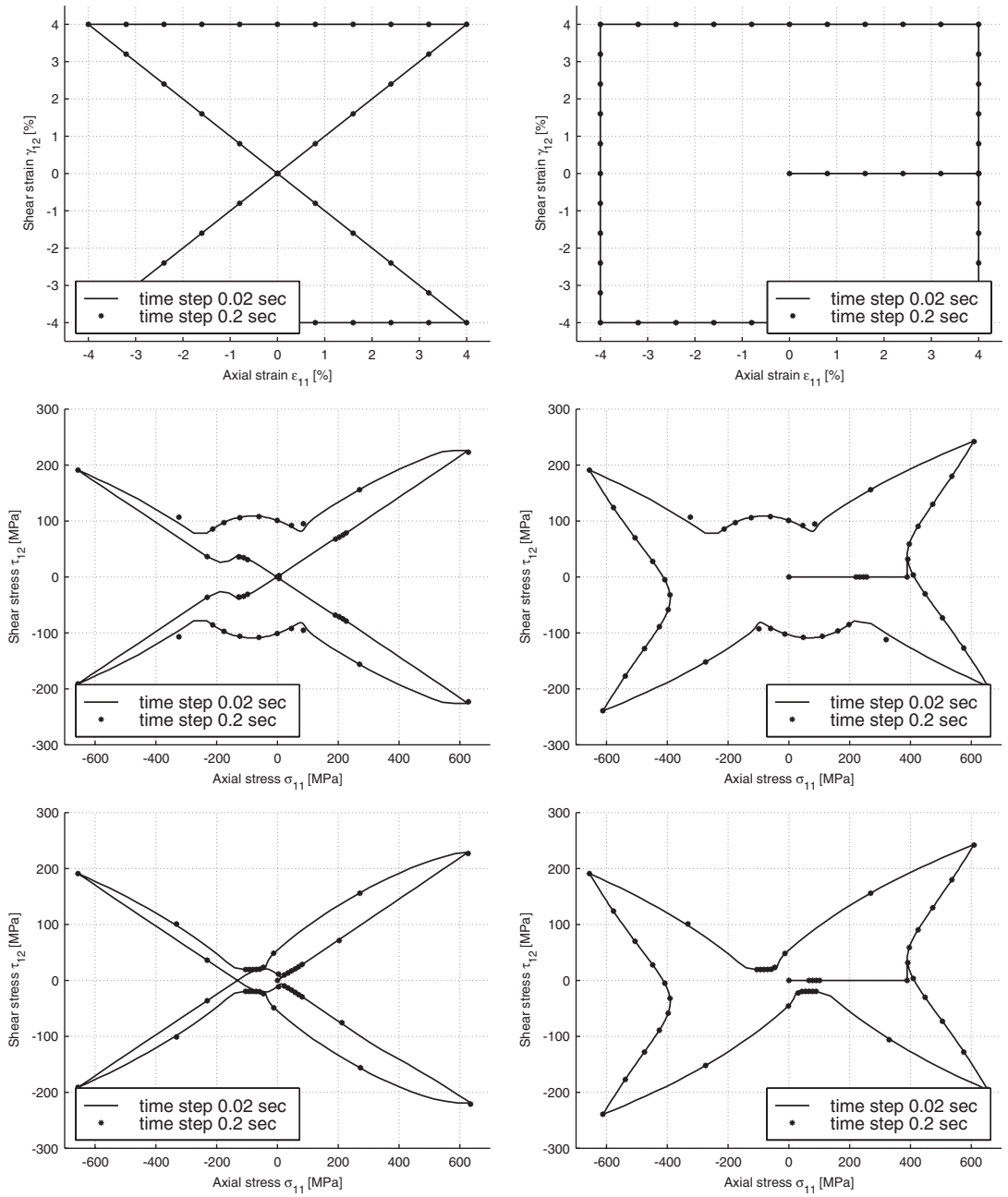

Figure 4. Biaxial test under strain control $\varepsilon_{11} - \gamma_{12}$. Hourglass-type strain history input (upper left) and square-type strain history input (upper right); stress history output at $T = 285$ K (centre); stress history output at $T = 223$ K (lower).

single-variant martensite is induced and the spring elongation is high. If the stress applied by the weight is less than the alloy recovery stress, heating the material above A_f induces the inverse ($SV \rightarrow A$) transformation and the spring lifts the weight. Moreover, cooling below M_f the transformation from austenite to single-variant martensite takes place and the weight stretches again the spring: accordingly, a repeatable two-way motion takes place.

To study this device, we consider a spring pinned at the top end, initially loaded by a vertical force at the bottom end (Figure 7(A)) and then, keeping constant the load, subjected to temperature cycles. The loading history is assumed as a linear function of the loading parameter $t \in [0, 8]$ s. and consists of five different stages, described in the following:

Time (s)	Loading history
$0 < t < 2$	The temperature is kept constant ($T = 210$ K) while the load is proportionally increased up to $F = 1.0$ N
$2 < t < 3$	The load is kept constant ($F = 1.0$ N) while the temperature is proportionally increased up to $T = 320$ K
$3 < t < 4$	The load is kept constant ($F = 1.0$ N) while the temperature is proportionally decreased up $T = 210$ K
$4 < t < 5$	The load and the temperature are kept constant ($F = 1.0$ N and $T = 210$ K)
$5 < t < 8$	The heating and cooling procedure is repeated

As already discussed, during the analysis of all the presented problems, we assume that during each time step the temperature is uniform in the material body, i.e. we neglect the thermo-mechanical coupling. The analysis is performed using the non-linear finite element code FEAP [41, 42], implementing the described algorithm into a user subroutine and employing 3D 8-node brick elements. In particular, the spring is meshed with 250 elements and 1020 nodes.

The material parameters are the ones presented in the previous section, except for the maximum transformation strain, ε_L, herein set equal to 7%.

Figure 7 presents the undeformed configuration ($t = 0$ s - picture A) as well as the deformed configuration at the end of the first step ($t = 2$ s - picture B), second step ($t = 3$ s - picture C) and third step ($t = 4$ s - picture D). It is evident the algorithm ability to describe the shape memory effect and to catch the typical behaviour of the actuator under heating–cooling cycles. Moreover, during the analysis a perfect quadratic convergence is obtained.

The actuator cyclic response is more evident in Figure 8, where we indicate with the letters A, B, C, D the points corresponding to the configurations shown in Figure 7. In the upper part of Figure 8 we plot the temperature input time history and the displacement output time history: we notice the displacement increment during force application at constant temperature and the following two-way motion during heating–cooling cycles. In the lower left part of Figure 8 we highlight the constant vertical reaction at the pinned edge due to the constant applied vertical load during the displacement variation induced by temperature changes. The displacement recovery is partial and, in this case, equal to the 88% of the total spring elongation. In the lower right part of Figure 8 we plot the displacement versus the temperature: it is evident the relationship between the displacement recovery and the transformation from martensite to austenite ($B \rightarrow C$) and, correspondingly, the relationship between the displacement increment and the transformation from austenite to martensite ($C \rightarrow D$). Finally, we note the model

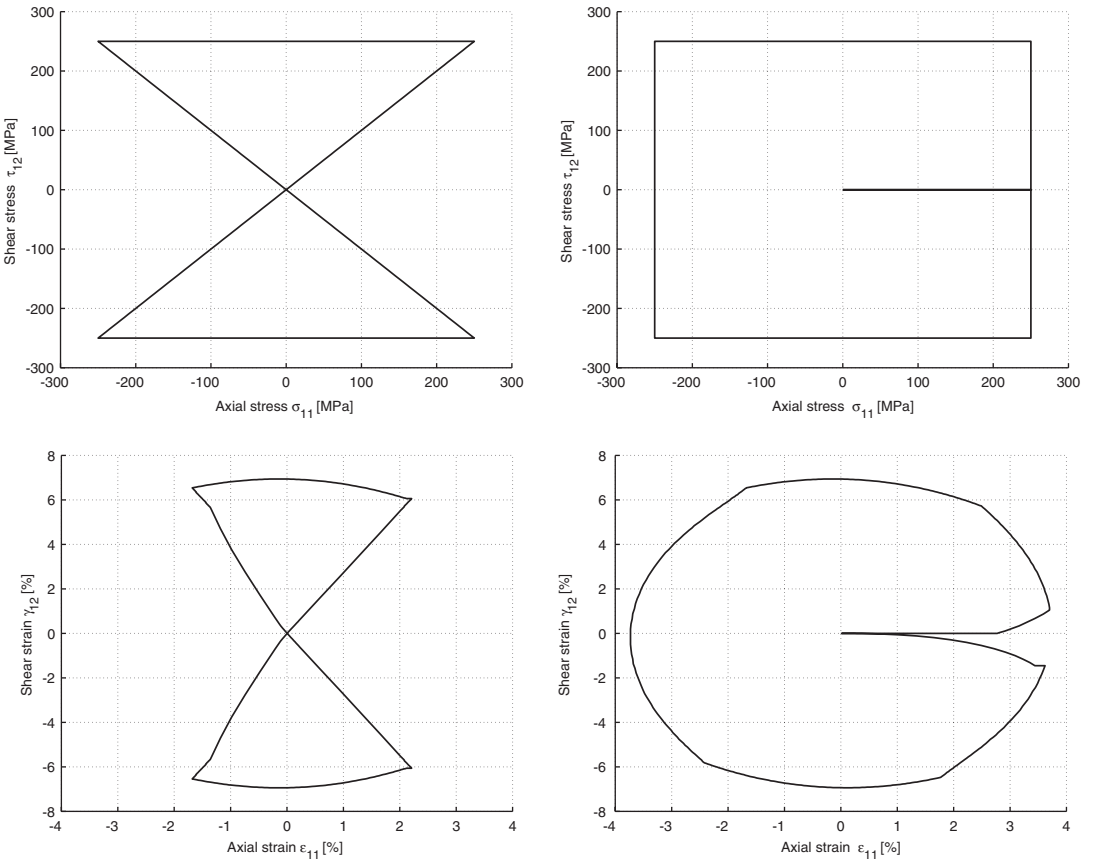

Figure 5. Biaxial test under stress control $\sigma_{11} - \tau_{12}$ at $T = 285\,\mathrm{K}$. Hourglass-type stress history input (upper left) and square-type stress history input (upper right); strain history output (lower).

capability to catch the A_f and A_s temperature dependency on the applied stress: in particular A_s is shifted from 248 to 274 K, A_f is shifted from 260 to 300 K.

4.2. Self-expanding stent

Between the several SMA devices employed in the biomedical field [43], self-expanding stent is probably one of the most diffused [44].

In general, stents are small tube-like structures used to recover and maintain the original shape of body conduit, such as bile ducts, blood vessels, esophagus and, with particular success, stenotic coronaries. In particular, this non-invasive cardiovascular surgery technique is routinely performed and it foresees the employment of balloon-expandable stainless-steel stents. Accordingly, the stent is mounted on a balloon, which is inflates to expand the device against the artery walls; plastically deformed during the balloon expansion, the stent remains in position, when the balloon is retreated, maintaining the artery open and restoring a blood flow (Figure 9).

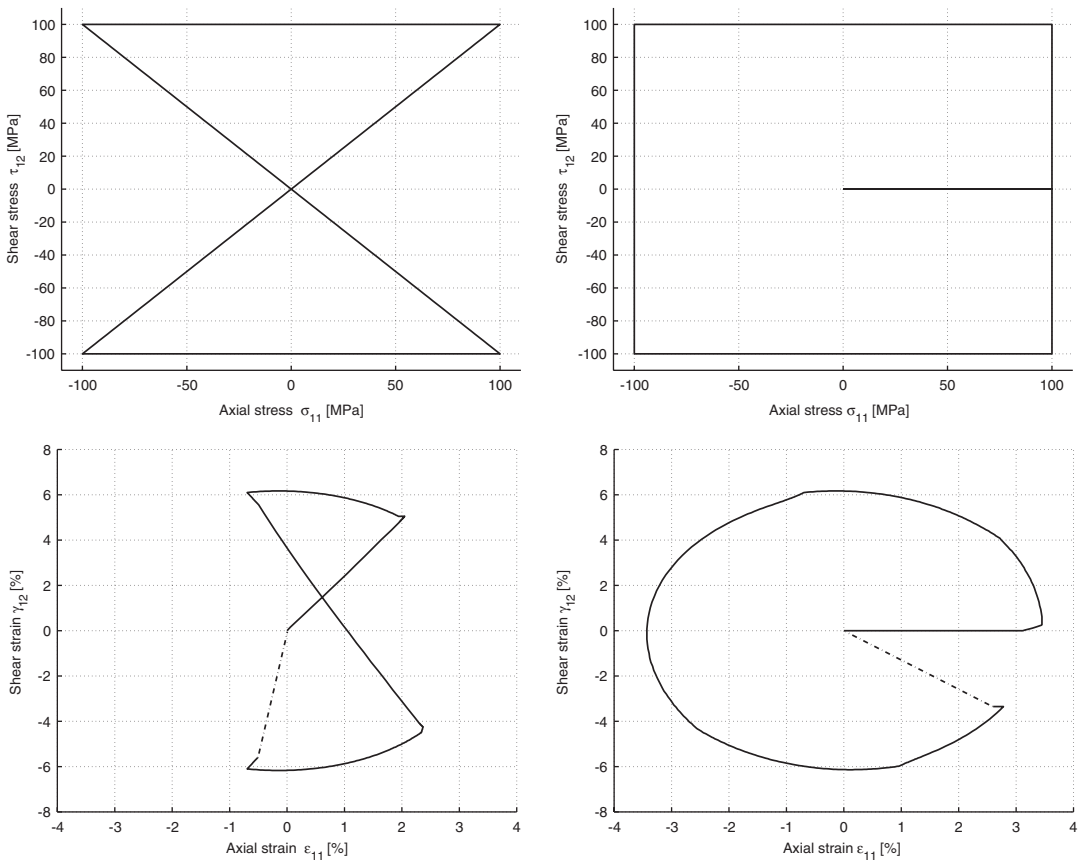

Figure 6. Biaxial test under stress control $\sigma_{11} - \tau_{12}$ at $T = 223\,\mathrm{K}$. Hourglass-type stress history input (upper left) and square-type stress history input (upper right); strain history output (lower) with strain recovery (dash–dot line) under temperature increment.

More recently there has been a proliferation of self-expanding SMA stents, exploiting the pseudo-elastic effect. Produced with the dimension of the healthy vessel diameter, SMA stents are initially inserted into the delivery system (crimping), and, once the constraint is removed, they self-expand (Figure 10). This approach allows some advantages with respect to balloon-expandable stents: a more flexible delivery system, a lower risk to overstretch the artery during expansion, a lower bending stresses when deployed in tortuous vessel.

However, the study of SMA stent is a highly non-linear problem due to design and material response complexity [45–47]. Hence, we now study the crimping and the free-expansion of a SMA stent. In a first step, we constrain all the stent nodes to move radially in order to describe the circumferential reduction associated to the crimping; in a second step we remove the radial constraints, letting the stent free to recover the undeformed shape. For the simulation we use the commercial non-linear finite element code ABAQUS (Hibbit Karlsson & Sorenses, Inc., Pawtucket, RI, U.S.A.), implementing the described algorithm into a user subroutine UMAT

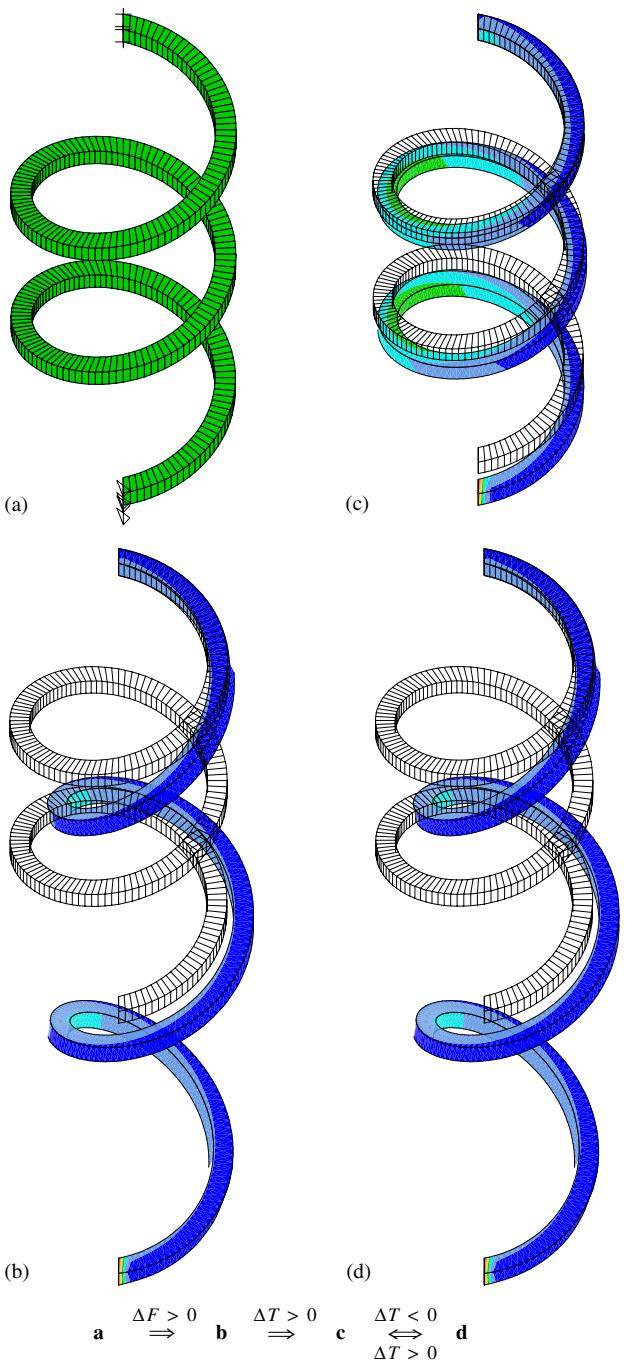

Figure 7. Spring actuator. Mesh and boundary conditions on the undeformed shape (A); deformed shape due to the weight application at $T < M_f$ (B); spring shape recovery and weight lifting due to heat above A_f (C); spring stretching due to cool above M_f under the weight action (D).

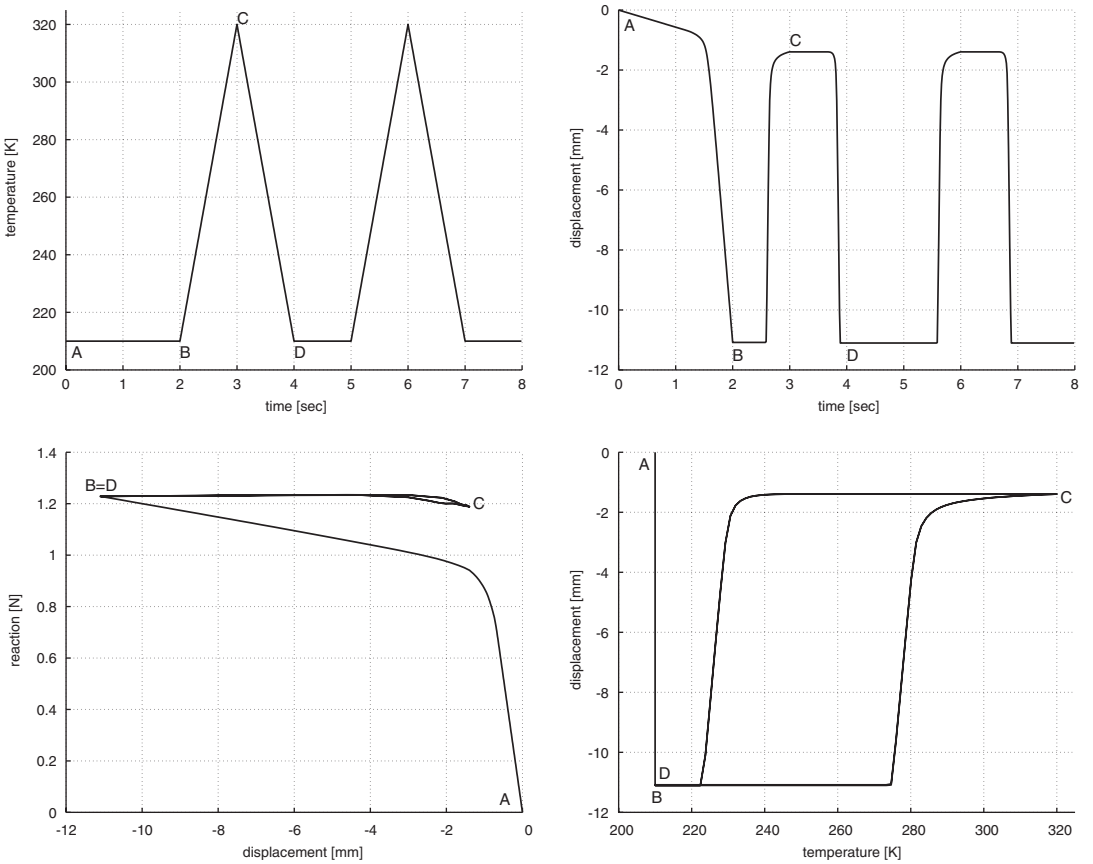

Figure 8. Spring actuator. Temperature input time history (upper left); vertical displacement output time history (upper right); vertical reaction of the upper pinned end versus vertical displacement of the lower loaded end during cycles (lower left); vertical displacement of the lower loaded end versus body temperature variation (lower right).

and employing for the analysis 3D 10-nodes tetrahedral elements. In particular, we create the model using the CAD program Rhinoceros 1.1 Evaluation (McNeel & Associates, Indianapolis, IN, U.S.A.), resembling only a portion (two rings and the relative links) of a real stent (SciMED Radius): in the undeformed configuration the stent model has a length of 5.2 mm, an outer diameter of 3.5 mm, a thickness of 0.2 mm (Figure 11). We automatically generate the mesh using the commercial code GAMBIT (Fluent Inc., Lebanon, NH, U.S.A.), obtaining a model with 33582 elements and 65952 nodes (a mesh detail is shown in the inset of Figure 11). The material parameters are the ones of the previous example.

Figure 12 presents the simulation results at the end of the crimping (first step—left part) and at the end of the free-expansion (second step—right part), in terms of deformed shape: the results show the algorithm capability to describe the pseudo-elastic effect and to self-expanding stent response. Also for this problem we verify a quadratic convergence during the overall analysis.

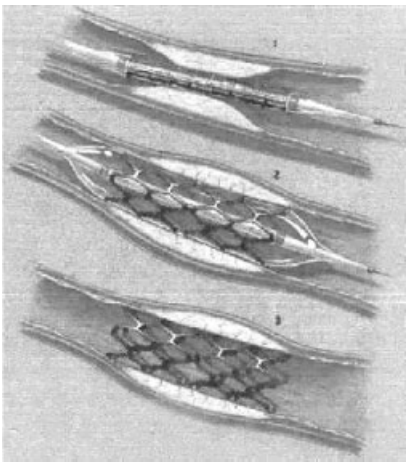

Figure 9. Technique performed to deploy stainless-steel stents: (1) the stent is positioned by a catheter into the stenotic area; (2) a balloon, placed inside the stent, inflates and expands the device against the vessel walls; and (3) the stent, plastically deformed during the expansion, remains in the position, when the balloon is retreated, and maintains the vessel open to restore the original blood flow (http://www.guidant.com).

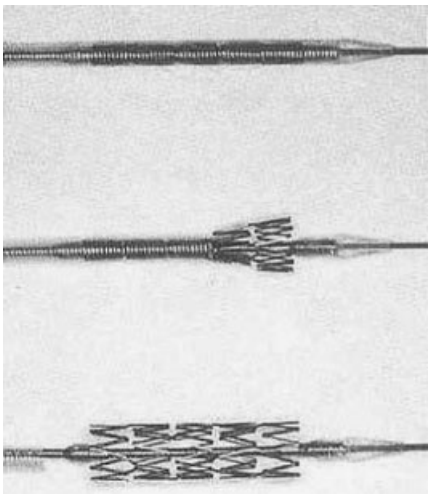

Figure 10. SMA self-expanding stent behaviour: (a) the stent is constrained by the catheter to reduce its diameter; (b) the catheter is partially removed and the stent tend to open; and (c) stent self-expansion once totally removed the catheter (http://www.medtronicave.com).

4.3. Coupling device for vacuum tightness

The first large scale application of SMA was a coupling device to connect titanium hydraulic tubing in a 1971 aircraft [48]. Nowadays, SMA couplings, fasteners and connectors are routinely

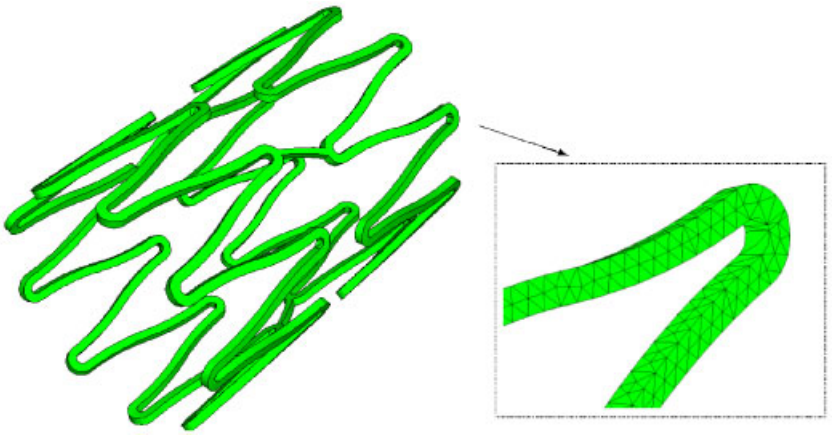

Figure 11. Self-expanding stent. Geometry of the undeformed shape and detail of the mesh.

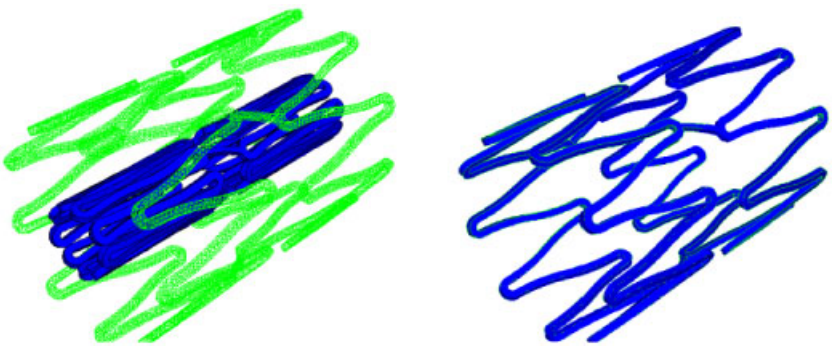

Figure 12. Self-expanding stent. Comparison between the deformed shape at the end of crimping and the initial undeformed shape (left); comparison between the deformed shape at the end of self-expanding and the initial undeformed shape (right).

used in many fields, all exploiting the force produced by a deformed SMA element when the original shape recovery is constrained [49].

In the following we numerically investigate the performance of a peculiar SMA coupling device, i.e. a vacuum tight shape memory flange to be used in the JET In-Vessel Inspection System [50]. In particular, we consider the first prototype [51], i.e a silica rod connected with a chamber where the vacuum has to be maintained. The connector is a flange in martensitic phase at ambient temperature realized welding two parts: the SMA sleeve, which constitutes the active part of the device, and the base, which is used to connect the flange to the rest of the apparatus. The sleeve has an initial diameter smaller than the rod diameter and it is radially deformed up to a diameter greater than the one of the rod. Hence, after positioning the flange around the rod, the transformation from martensite to austenite is induced heating the material. The rod constrains the flange shape recovery, which is able to apply a pressure on the rod, assuring a good leak rate.

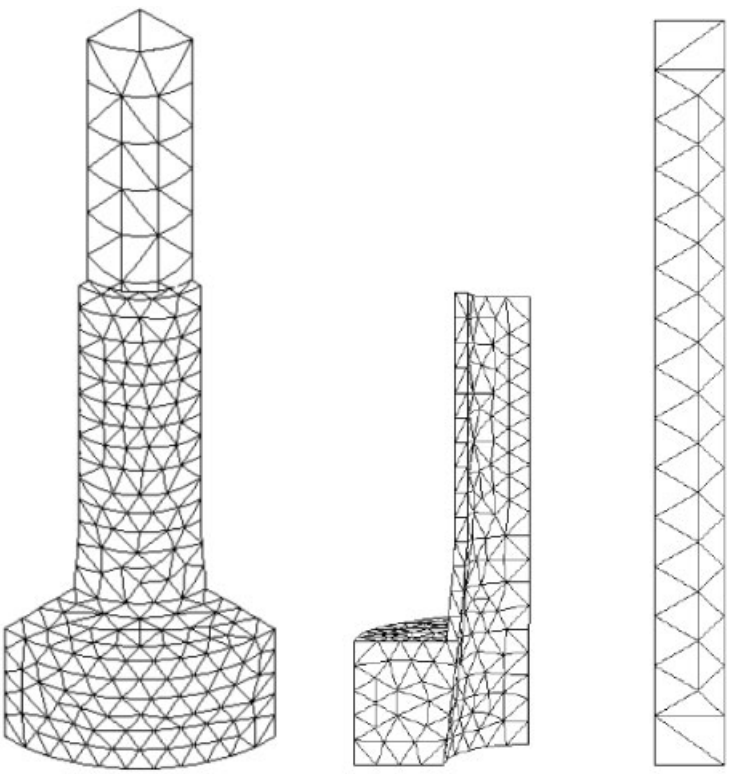

Figure 13. Vacuum flange to be fixed around a silica rod for IVIS of JET. Geometries and meshes of the flange and rod in the working position (left) and exposed in the separated components (right).

We study the initial flange enlargement and the following constrained shape recovery by finite element method. We use the ABAQUS code both for creating the model and running the analysis employing the user subroutine UMAT and the code tool 'CONTACT'. The model consists of 764 3D 10-nodes tetrahedral elements and 1637 nodes: the symmetry of the structure allows to study only a quarter (Figure 13). Also in this example we use the SMA material parameters previously introduced. The silica behaviour is described by a linear isotropic elastic constitutive model: the Young's modulus is assumed equal to 74 000 MPa and the Poisson's ratio equal to 0.2.

In the first step of the analysis, we apply a linearly increasing pressure along the sleeve internal face to simulate the enlargement of the SMA sleeve diameter: we maintain constant the temperature ($T = 223\,\mathrm{K} = M_\mathrm{f}$) and we do not activate the rod-sleeve contact. In the second step we remove the pressure, we activate the contact between the rod and the sleeve and we heat the material up to a temperature above A_f, inducing shape recovery. When the sleeve enters in contact with the rod, the recovery is constrained and hence the SMA flange applies a contact pressure on the rod. The maximum strain reached during the expansion does not overcome the limit strain ($\varepsilon_\mathrm{L} = 7\%$) and the constrained recovery takes place at a strain of

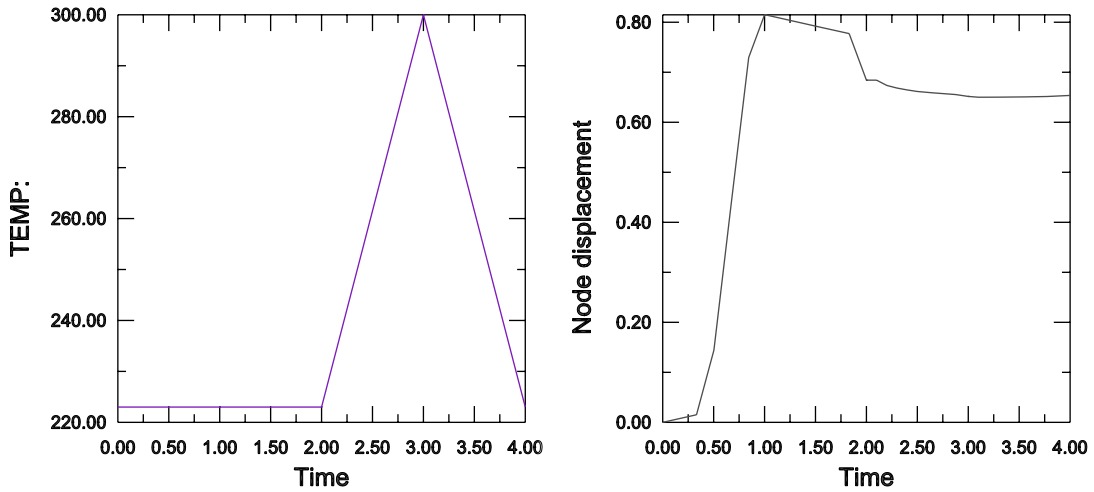

Figure 14. Vacuum tight flange. Temperature time history (left part) and corresponding displacement history of a point at the top of the SMA sleeve (right part).

4.5%. Figure 14 depicts the temperature time history as well as the corresponding displacement for a point at the top of the SMA sleeve.

The results show the algorithm capability to describe the one-way shape memory effect and to catch the constrained recovery effect. Also in this case we verify a quadratic convergence during the overall analysis.

5. CLOSURE

In the past, the research on Shape Memory Alloys was mainly devoted, on one hand, to the experimental observation of the material behaviour, on the other hand, to the formulation of constitutive models. Nowadays, with the wide diffusion of SMA devices in many fields, as biomedical, mechanical, civil, aerospatial and automotive engineering, it has been recognized the fundamental contribution of numerical analysis, in particular of the finite element method, in the exploitation of SMA peculiar features and in the design of SMA devices. Accordingly, the development of numerical algorithms for the proposed SMA constitutive models becomes a very important aspect.

In this paper, we consider an effective 3D SMA constitutive model and we pay attention to the time-discrete counterpart as well as to the consistent tangent matrix.

We check the numerical algorithm capability and efficiency performing uni-axial as well as multi-axial non-proportional tests. Finally, we show that the proposed model is a valid instrument for the design of SMA devices; indeed we verify the computational tool ability to simulate the behaviour of three SMA applications: a spring actuator, a self-expanding stent, a coupling device for vacuum tightness. In particular, in the first case the model is able to catch the two-way shape-memory induced by a bias force, in the second case it is able to describe

the classical pseudo-elastic effect as well as in last case the one-way shape-memory effect with constrained recovery.

ACKNOWLEDGEMENTS

The present work has been partially developed within the joint French–Italian 'Lagrange laboratory' project as well as partially supported by the Ministero dell'istruzione, dell'università e della ricerca (MIUR) through the research program 'Shape-memory alloys: constitutive modeling, structural behaviour, experimental validation and applicability to innovative biomedical applications' and through the program of collaboration between CNR and MIUR (law 449/97).

We wish to thank Doctor Nunzio Valoroso (Consiglio Nazionale delle Ricerche, Roma) for his help in the SMA constitutive model improvement.

REFERENCES

1. Kurdjumov GV, Sachs G. *Zeitschrift für Physik* 1930; **64**:325.
2. Otsuka K, Shimizu K. Pseudoelasticity and shape memory effects in alloys. *International Metals Reviews* 1986; **31**:93–114.
3. Funakubo H. *Shape Memory Alloys*. Gordon and Breach: London, 1987 (Translated from the Japanese by J.B. Kennedy.).
4. Wayman CM. Shape memory and related phenomena. *Progress in Materials Science* 1992; **36**:203–224.
5. Wollants P, Roos JR, Delaey L. Thermally- and stressed-induced thermoelastic martensitic transformations in the reference frame of equilibrium thermodynamics. *Progress in Materials Science* 1993; **37**:227–288.
6. Müller I. Thermodynamics of ideal pseudoelasticity. *Journal de Physique IV* 1995; **C2-5**: 423–431.
7. Nishimura F, Watanabe N, Watanabe T, Tanaka K. Transformation conditions in an Fe-based shape memory alloy under tensile-torsional loads: martensite start surface and austenite start/finish planes. *Material Science and Engineering* 1999; **A264**:232–244.
8. Miyazaki S. Development and characterization of shape memory alloys. In *CISM Courses and Lectures: Shape Memory Alloys*, vol. 351. Springer: Wien, NewYork, 1996; 69–143.
9. Leo PH, Shield TW, Bruno OP. Transient heat transfer effects on the pseudoelastic behavior of shape-memory wires. *Acta Metallurgica Materialia* 1993; **41**:2477–2485.
10. Shaw JA, Kyriakides S. Thermomechanical aspects of NiTi. *Journal of the Mechanics and Physics of Solids* 1995; **43**:1243–1281.
11. Lim TJ, McDowell DL. Mechanical behavior of an Ni–Ti alloy under axial-torsional proportional and non-proportional loading. *Journal of Engineering Materials and Technology* 1999; **121**:9–18.
12. Kim SJ, Abeyaratne R. On the effect of the heat generated during stress-induced thermoelastic phase transformation. *Continuum Mechanics and Thermodynamic* 1995; **7**:311–332.
13. Chrysochoos A, Pham H, Maissonneuve O. Energy balance of thermoelastic martensite transformation under stress. *Nuclear Engineering and Design* 1996; **162**:1–12.
14. Ranieki B, Tanaka K, Ziolkowski A. Testing and modeling of NiTi SMA at complex stress state—selected results of polish-Japanese research cooperation. *Material Science Research International, Special Technical Publication* 2001; **2**:327–334.
15. Tanaka K, Kobayashi S, Soto Y. Thermomechanics of transformation pseudoelasticity and shape memory effect in alloys. *International Journal of Plasticity* 1986; **2**:59–72.
16. Brinson LC. One-dimensional constitutive behavior of shape memory alloys: thermomechanical derivation with non-constant material functions and redefined martensite internal variables. *Journal of Intelligent Material Systems and Structures* 1993; **4**:229–242.
17. Auricchio F. Considerations on the constitutive modeling of shape-memory alloys. In *Shape Memory Alloys: Advances in Modelling and Applications*, Auricchio F, Faravelli L, Magonette G, Torra V (eds). CMINE: Barcelona, 2002; 125–187.
18. Duerig TW, Melton KN, Stökel D, Wayman CM (eds). *Engineering Aspects of Shape Memory Alloys*. Butterworth-Heinemann: Stoneham, MA, 1990.
19. van Moorleghem W, Besselink P, Aslanidis D (eds). *SMST-Europe 1999*, Antwerp Zoo, Belgium, 1999. CD-ROM only.

20. Russel SM, Pelton AR (eds). *Proceedings of the Third International Conference on Shape Memory and Superelastic Technologies*, Asilomar, CA, 2000.
21. Russel SM, Pelton AR (eds). *Proceedings of the Fourth International Conference on Shape Memory and Superelastic Technologies*, Asilomar, CA, 2003.
22. Souza AC, Mamiya EN, Zouain N. Three-dimensional model for solids undergoing stress-induced phase transformations. *European Journal of Mechanics, A: Solids* 1998; **17**:789–806.
23. Auricchio F, Petrini L. Improvements and algorithmical considerations on a recent three-dimensional model describing stress-induced solid phase transformations. *International Journal for Numerical Methods in Engineering* 2002; **55**:1255–1284.
24. Lubliner J. *Plasticity Theory*. Macmillan: New York, 1990.
25. Orgéas L, Favier D. Non-symmetric tension-compression behavior of NiTi alloy. *Journal de Physique IV*, 1995; **C8**:605–610.
26. Leclercq S, Lexcellent C. A general macroscopic description of the thermomechanical behavior of shape memory alloys. *Journal of Mechanics and Physics of Solids* 1996; **44**:953–980.
27. Fremond M. Shape memory alloy. A thermomechanical macroscopic theory. In *CISM Courses and Lectures: Shape Memory Alloys*, vol. 351. Springer: Wien, NewYork, 1996; 1–68.
28. Gall K, Sehitoglu H, Chumlyakov YI, Kireeva IV. Tension-compression asymmetry of the stress–strain response in aged single crystal and polycristalline NiTi. *Acta Materialia* 1999; **47**:1203–1217.
29. Patoor E, Eberhardt A, Berveiller M. Micromechanical modelling of superelasticity in shape memory alloys. *Journal de Physique IV* 1996; **C1-6**:277–292.
30. Manach PY, Favier D. Shear and tensile thermomechanical behavior of equiatomic NiTi alloy. *Materials Science and Engineering* 1997; **A222**:45–57.
31. Freudenthal AM, Gou PF. Second order effects in the theory of plasticity. *Acta Mechanica* 1969; **8**:34–52.
32. Auricchio F, Petrini L, Peyroux R. Modeling shape memory alloys: dissipative versus non-dissipative behaviors. In *XVI Congresso AIMETA di Meccanica Teorica e Applicata*, 2003; 1–10.
33. Peyroux R, Chrysochoos A, Licht C, Lobel M. Thermomechanical couplings and pseudoelasticity of shape memory alloys. *International Journal of Engineering Science* 1998; **36**:489–509.
34. Crisfield MA. *Non-linear Finite Element Analysis of Solids and Structures*. Wiley: New York, 1996.
35. Simo JC, Hughes TJR. *Computational Inelasticity*. Springer: Berlin, 1998.
36. Simo JC. Topics on the numerical analysis and simulation of plasticity. In *Handbook of Numerical Analysis*, Ciarlet PG, Lions JL (eds), volume III. Elsevier Science Publisher: Amsterdam, 1999.
37. Helm D, Haupt P. Shape memory behaviour: modelling within continuum thermomechanics. *International Journal of Solids and Structures* 2003; **40**:827–849.
38. Sittner P, Hara Y, Tokuda M. Experimental study on the thermoelastic martensitic transformation in shape memory alloy polycrystal induced by combined external forces. *Metallurgical and Materials Transactions* 1995; **26A**:2923–2935.
39. Duerig TW, Stökel D, Keeley A. Actuator and work production devices. In *Engineering Aspects of Shape Memory Alloys*, Duerig TW, Melton KN, Stökel D, Wayman CM (eds). Butterworth-Heinemann: London, 1990; 181–194.
40. Liang C, Rogers CA. Design of shape memory alloy actuators. *Journal of Intelligent Material Systems and Structures* 1997; **8**:303–313.
41. Zienkiewicz OC, Taylor RL. *The Finite Element Method*, 5th edn, vol. I. Butterworth-Heinemann: New York, 2000.
42. Zienkiewicz OC, Taylor RL. *The Finite Element Method*, 5th edn, vol. II. Butterworth-Heinemann: New York, 2000.
43. Lipscomb IP, Nokes LDM. *The Application of Shape Memory Alloys in Medicine*. Mechanical Engineering Publications Limited: U.K. 1996.
44. Melzer A, Stökel D. Performance improvement of surgical instrumentation through the use of Ni–Ti materials. In *Proceedings of the First International Conference on Shape Memory and Superelastic Technologies*, Asilomar, CA, Pelton AR, Hodgson D, Duerig T (eds). SMST International Comittee: Pacific Grove, CA, 1994; 401–409.
45. Dumoulin C, Cochelin B. Mechanical behaviour modelling of balloon-expandable stents. *Journal of Biomechanics* 2000; **33**:1461–1470.
46. Etave F, Finet G, Boivin M, Boyer JC, Rioufol G, Thollet G. Mechanical properties of coronary stents determined by using finite element analysis. *Journal of Biomechanics* 2001; **34**:1065–1075.

47. Migliavacca F, Petrini L, Colombo M, Auricchio F, Pietrabissa R. Mechanical behavior of coronary stents investigated through the finite element method. *Journal of Biomechanics* 2002; **35**:803–811.
48. Van Humbeeck J. Non-medical applications of shape memory alloys. *Materials Science and Engineering* 1999; **A273-275**: 134–148.
49. Kapgan M, Melton KN. Shape memory alloy tube and pipe coupling. In *Engineering Aspects of Shape Memory Alloys*, Duerig TW, Melton KN, Stökel D, Wayman CM (eds). Butterworth-Heinemann: London, 1990; 137–148.
50. Besseghini S, Ceresara S, Tuissi A. Developing of a shape memory vacuum thight flange. *Report R-97/10*, Istituto per la tecnologia dei materiali metallici non tradizionali, Consiglio Nazionale delle Ricerche, 1997.
51. Besseghini S, Ceresara S, Tuissi A. Feasibility test of memory alloy vacuum thight flanged collers for IVIS (Internal Vessel Inspection System) of JET. *Report R-96/7*, Istituto per la tecnologia dei materiali metallici non tradizionali, Consiglio Nazionale delle Ricerche, 1996.

